Title

Establishing a unified framework for ion solvation and transport in liquid and solid electrolytes

Journal

Trends in Chemistry, 3(10)

ISSN

2589-7209

Authors

Siegel, Donald J

Nazar, Linda

Chiang, Yet-Ming

et al.

Publication Date

2021-10-01

DOI

10.1016/j.trechm.2021.06.004

Establishing a Unified Framework for Ion Solvation and Transport in Liquid and Solid Electrolytes

Donald J. Siegel,[1,6] Linda Nazar,[2,6] Yet-Ming Chiang,[3,6] Chao Fang,[4,6] Nitash P. Balsara[4,5,6]

[1] Mechanical Engineering, Materials Science & Engineering, and Applied Physics Program, University of Michigan, Ann Arbor, MI 48109, USA

[2] Department of Chemistry, Department of Chemical Engineering, and the Waterloo Institute of Nanotechnology, University of Waterloo, Ontario Canada N2L 3G1

[3] Department of Materials Science and Engineering, Massachusetts Institute of Technology, Cambridge, MA 02139, USA

[4] Materials Sciences Division, Lawrence Berkeley National Lab, Berkeley, CA 94720, USA

[5] Department of Chemical and Biomolecular Engineering, University of California, Berkeley, CA 94702, USA

[6] Joint Center for Energy Storage Research, Argonne National Laboratory, Lemont, IL 60439, USA

Abstract

Electrolytes used in rechargeable batteries must enable rapid translation of the working ion from between the electrodes. They are, however, usually designed and synthesized using atomic-level insights. Whether the ideal electrolyte for a particular battery is a solid or a liquid remains an important unresolved question, especially as solids with conductivities comparable to liquids are discovered. To help resolve such questions, we present the first steps toward a cross-cutting unified framework for relating atomic and continuum scale phenomena. Solvation *shells* in liquids are entities that translate with the working ion for a short while before they break up due to Brownian motion. In contrast, solvation *cages* in classical solids and polymers cannot not translate with the working ion. Mobility of the entities that make up the cages and shells, quantified by an order parameter, is shown to influence translation of the working ion on continuum length scales.

Keywords: solids; liquids; electrolytes; solvation; ion transport; shells; cages

Liquid *versus* solid electrolytes

The performance of electrochemical systems such as batteries, hydrogen and solid oxide fuel cells, and electrochemical reactors for production of materials such as aluminum and chlorine depend on the transport of specific working ions across an electrolyte [1]. In the relatively simple case of a lithium-ion battery, a single working ion, Li^+, participates in the redox reactions at both electrodes [2]. Other systems such as the lead acid battery are more complex, and both cations and anions (H^+ and SO_4^{2-}) participate in the redox reactions. It has long been recognized that the electrolyte can, in principle, be either a liquid or a solid [3].

The kind of electrolytes that will be used in electrochemical systems to propel the emerging clean energy translation remains undecided [4]. For many decades, efforts aimed at achieving ionic **conductivity** (see Glossary) in bulk solids comparable in magnitude to that of liquid electrolytes yielded little progress. A breakthrough was reported in 2011 with the discovery of $Li_{10}GeP_2S_{12}$ [5]. Moreover, the recent discovery of a number of ion-conducting solids with conductivities [6-10] equaling that of liquids [11],[12] has generated intense interest in the development of all-solid-state batteries [13]. Indeed, research and development on solid-state batteries is arguably the most hotly pursued area in the modern battery space. Diligent efforts are taking place at academic and national research laboratories, established battery producers, and numerous battery start-ups to bring all-solid lithium batteries to the market [14-16].

In addition to conducting ions rapidly, the deformability and adhesion of the electrolyte to solid electrode surfaces, usually redox-active particles as they expand and contract during charge and discharge, is an important characteristic [17-21]. For rigid solid electrolytes, coupled mechanical and electrochemical stability, especially against penetration by metal protrusions and dendrites, remains unresolved [18,22-27]. Drawbacks of liquid-based systems include flammability of organic solvents often used when the working ion is an alkali metal, and the potential for catastrophic failure if the liquid is displaced and the electrodes short circuit. These drawbacks can, in principle, be addressed by solid electrolytes, if issues related to deformability and adhesion can be addressed [17-20]. Toward the goal of enabling solid-state batteries, the purpose of this perspective is to explore the possibility of developing a unified framework for describing ion transport that bridges the gap between apparently dissimilar liquid and solid electrolytes. Generally speaking, research on these two classes of materials is carried out in distinct camps with their own conventions and nomenclatures. The proposed framework is built on the concepts of solvation **shells** and **cages**. For coherence and due to their relevance in practical systems, we have chosen examples wherein the working ion is a lithium cation. We posit that the development of new and improved electrolytes will be accelerated by understanding both similarities and differences across different classes of ion conductors.

Shells and cages

As an organizing concept, we use the term shell to describe the solvation structure in liquids, and cage to describe the solvation structure in polymers and crystals. Solvation of cations in liquid electrolytes is enabled by the presence of electronegative groups in the solvent molecules [11,28]. The dominant solvation shell that surrounds a Li^+ ion in a dilute aqueous mixture of lithium bis(trifluoromethanesulfonyl)imide (LiTFSI) is shown in Figure 1a. The dominant solvation shell has, to a reasonable approximation, tetrahedral symmetry with oxygen atoms at the apices of the tetrahedron [29],[30].

In Figure 1b, we show the structure of β-Li_3PS_4 (LPS), a fast-ion conducting solid that is thermodynamically stable in its bulk crystalline form only above 200 °C, although a nanoporous phase is stable at room temperature [31]. β-Li_3PS_4 exhibits a different $[PS_4]^{3-}$ motif, Li^+ ion environment and expanded cell volume, compared to non-conductive γ-LPS (the room temperature phase) [32], While both solids can be described as having Li^+ ions contained within solvation cages formed by sulfide (S^{2-}) ions, the frameworks of the β- and γ-phases differ greatly. The latter contains tetrahedral LiS_4 cages whose S^{2-} apices are shared with the PS_4^{3-} moieties, whereas the β-phase comprises both octahedral (LiS_6) and tetrahedral (LiS_4) cages that share edges with the PS_4^{3-} framework. The bulk crystalline β-phase can be stabilized at room temperature by the substitution of P^{5+} for Si^{4+} to form $Li_{3.25}[P_{3/4}Si_{1/4}]S_4$ [33], where the additional Li^+ ions needed for charge balance expand the cell volume even beyond β-LPS. The solvation cage structure, its connectivity to the framework, and lattice volume are important with respect to coupling to (and triggering) anion dynamics as we describe below.

Inorganic glasses constitute another class of practically-relevant solid ion conductors [34-36]. The amorphous nature of glasses implies the potential for significant variability in the solvation structure of the working ion; this behavior is fundamentally different from the periodicity and order in the cages of crystalline materials [37,38]. Glasses are similar to crystalline conductors in that the ions comprising the solvation cage do not execute Brownian diffusion. However, glasses are defined by both structural and dynamic heterogeneity [39,40]: the working ions are surrounded by different solvation motifs that are characterized by **amorphous halos** in X-ray diffraction experiments, and regions composed of rapidly moving **entities** coexist with regions wherein the same entities are jammed and thus immobile. The absence of well-defined long-range order makes the modeling of glasses challenging [38]. Figure 1c illustrates the atomic structure of an inorganic, ion-conducting glass [41], referred to here as glassy LPS, generated by heat-and-quench *ab initio* molecular dynamics simulations (AIMD) [42]. LPS glass is synthesized by combining Li_2S and P_2S_5 in a 75%:25% ratio [40]; the glass is the amorphous analogue of the crystalline polymorphs β and γ-Li_3PS_4 discussed above. Similar to those crystalline phases, the glass contains tetrahedral PS_4^{3-} complex anions. Different from those phases, in the glass, the number and orientation of anions that coordinate the working Li^+ ion varies from cation to cation.

Polymer electrolytes also possess polyhedral cages. In Figure 1d, we show the solvation structure that surrounds a dissociated Li^+ ion in an amorphous mixture of LiTFSI and polyethylene oxide (PEO); polymer electrolytes typically exhibit reasonable conductivities at elevated temperatures. The dominant solvation cage has, to a reasonable approximation, octahedral symmetry. A majority of the ether oxygens that form the cage belong to one or two chain molecules [43-47].

Cage mobility as an order parameter

In order to enable electrolytic charge transport under applied electric fields, the working ion must, in the absence of electric fields, exhibit diffusive motion in the long-time limit, *i.e.*, the ensemble-averaged mean-squared displacement of the working cation is a linear function of time, t. The crystalline and glassy solids in Figure 1 only contain cations and anions while the other two electrolytes also contain a solvent. The subscripts $i = 0$, + and – refer to the solvent molecules or monomers along the polymer chains, cations, and anions, respectively. The individual entities (ions, solvent molecules, or monomers) are labeled β (and γ when two labels are necessary) and

N_i is the total number of entities of type i in the system. If the location of each entity is $\boldsymbol{r}_i^{\beta}$, then the ensemble-averaged mean-squared displacement, $< \Delta r_i^2(t) >$, is given by

$$< \Delta r_i^2(t) >= \frac{\langle \sum_{\beta=1}^{N_i} \left(\boldsymbol{r}_i^{\beta}(t) - \boldsymbol{r}_i^{\beta}(0)\right).\left(\boldsymbol{r}_i^{\beta}(t) - \boldsymbol{r}_i^{\beta}(0)\right) \rangle}{N_i}. \quad (1)$$

The time dependence of $<\Delta r_+^2>$ of the working ion is qualitatively similar for all the electrolyte classes depicted in Figure 1. The distinction between the different classes becomes clear when we examine the time dependence of $< \Delta r_i^2(t) >$ of other entities. Different species exhibit different power laws,

$$< \Delta r_i^2(t) >= D_i t^{\alpha_i}, \quad (i = 0, +, \text{or } -). \quad (2)$$

The parameter D_i reduces to $6D_{self,i}$ in the limit $t \to \infty$ if the species i exhibits diffusive motion and $D_{self,i}$ is the self-diffusion coefficient. For all of the electrolytes in Figure 1, $\alpha_+ = 1$.

In liquids, the solvation structure can be "carried" by the ion as it translates across space. However, the random Brownian motion of all entities results in frequent alterations of the solvation structure. Solvation *shells*, as we define them here, are structures that are capable of breaking up and reforming. In Figure 2b we show $< \Delta r_i^2(t) >$ based on molecular dynamics simulations [29,30] for a mixture of LiTFSI and water. In liquid electrolytes, all three species exhibit diffusive behavior with $\alpha_i = 1$. The ions find themselves in a multitude of environments but traverse rapidly through them to yield trajectories that are averaged over these environments. In the other electrolytes in Figure 1, however, we obtain different relationships between mean-squared displacement and time.

In classical solid electrolytes (both crystals and glasses), the solvation structures do not translate, hence $<\Delta r_i^2>$ of the cage entities is independent in the limit $t \to \infty$. Solvation *cages* are thus defined as structures that exhibit sub-diffusive motion on the time scale of working ion diffusion. We show the time dependence of $<\Delta r_-^2>$ for the negatively charged cage elements of glassy LPS obtained by AIMD simulations in Figure 2c. The simulations were carried out at 500 K so that diffusive regimes could be accessed within the simulations time scale. On the $t > 0.5$ ns time scale, where the cations show diffusive behavior ($\alpha_+ = 1$), the anions in the cages are characterized by $\alpha_- = 0$.

The case of a polymeric ion conductor is intermediate between classical liquids and solids. We limit our discussion to amorphous polymers that are well-above their glass transition temperature. On long-enough time scales, polymer chains in amorphous melts exhibit diffusive motion. However, the diffusion of polymer chains is much slower than that of small molecules (such as water), and the solvation cage remains essentially intact on the time scale of cation motion. In Figure 2d we show MD simulation results for a mixture of LiTFSI and PEO [48]. The $TFSI^-$ anions exhibit diffusive motion on the $t > 5$ ns time scale, while time scales greater than 1000 ns are necessary for Li^+ cations to exhibit diffusive motion; this time scale is often outside the range of MD simulations. On these time scales, the PEO monomers exhibit a power law with $\alpha_0 = 0.5$. At a coarse-grained level, polymer chains can be modeled as beads connected by springs, and the collective motion of the springs on short time scales give an exponent of 0.5 [46].

We define an order parameter, M, to characterize the mobility of the entities in the solvation cages or shells

$$M = \frac{\alpha_i}{\alpha_+} = \alpha_i \,, (i \neq +) \quad (3)$$

where α_i is the exponent of the power law relationship between $<\Delta r_i^2>$ and t. The mobility order parameter lies between 0 and 1: liquid electrolytes exhibit M values of 1, inorganic solids exhibit M values of 0, and polymer electrolytes exhibit M values of 0.5. Other forms of matter such as liquid crystalline electrolytes may exhibit other values of M.

In addition to translational displacement of the cage entities, recent work indicates that the diffusion of the cations in both crystalline and glassy LPS is facilitated by the *rotation* of the anions in the cages. For example, in Figure 2c we show the mean-squared angular displacement, $< \Delta\theta_-^2(t) >$ of the anions in glassy LPS as a function of time, obtained by AIMD simulations. The linear dependence of $< \Delta\theta_-^2(t) >$ on time indicates free rotational diffusion of the anions in the cage. It is, in this case, appropriate to expand our definition of M to include rotational dynamics,

$$< \Delta\theta_i^2(t) >= D_{\theta,i} t^{\alpha_{\theta,i}}, \quad (4)$$

and we define the rotational order parameter as

$$M_\theta = \frac{\alpha_{\theta,i}}{\alpha_+} = \alpha_{\theta,i}. \quad (5)$$

The values of M (and M_θ when relevant) for the four examples in Figure 1 are presented in Table 1.

Relationship between ion transport and cage dynamics

The connection between displacement of charged species and ion transport in isotropic electrolytes comprising a solvent and two mobile charged species (Figures 1a and 1d) was developed formally by Onsager [49]. In this framework, ion transport is governed by transport coefficients that we now refer to as **Onsager coefficients**, $\boldsymbol{L_{ij}}$. While several approaches for determining these coefficients have been published [50-54], a particularly transparent approach was recently proposed by Fong and colleagues [55], who derived the following expression for L_{ij},

$$L_{ij} = \frac{1}{6k_B TV} \lim_{t\to\infty} \left[\frac{\partial}{\partial t} \left(< \sum_{\beta=1}^{N_i} \left(\boldsymbol{r}_i^\beta(t) - \boldsymbol{r}_i^\beta(0) \right) . \sum_{\gamma=1}^{N_j} \left(\boldsymbol{r}_j^\gamma(t) - \boldsymbol{r}_j^\gamma(0) \right) > \right) \right],$$

$$(i, j \ = + \text{ or } -) \quad (6)$$

where k_B is the Boltzmann constant, T is the temperature, and V is the volume of the system. The extent to which the different approaches [50-55] in the literature are consistent with each other remains to be established.

On the continuum scale, coefficients L_{ij} relate the flux of species i to gradients in the chemical potentials of species j [49]. While the three Onsager coefficients can be calculated using simulations as described above, they are difficult to measure by direct experimentation. Newman developed strategies for measuring three different transport properties – ionic conductivity, **salt diffusion coefficient**, and the **cation transference number** [1,77]. Relationships between the experimentally measured transport parameters and the Onsager coefficients can be found in the

literature (e.g., conductivity, $\kappa = F^2 \sum_i \sum_j z_i z_j L_{ij}$; F is the Faraday constant and z_i is the charge number on species i) [1,55]. While coefficients L_{ij} depend on the choice of the reference frame, some properties like conductivity are invariant with respect to this choice while others like the transference number are not.

In crystals and glasses (Figures 1b,c), only cations exhibit translational motion and thus only L_{++} is relevant (rotation is not relevant in the Onsager framework). Other systems that fall within this class are pure ionic liquids and molten salts [1]. In crystals, ion transport has classically been modeled in terms of activation barriers that present themselves as the ion hops from one unit cell to the next [56]. In the simplest cases, the cations translate over a saddle-point that determines the height of the barrier. The saddle-point is typically a triangular window spanned by the anions which constitute the faces in the tetrahedral or octahedral solvation cage of the cation that creates a bottleneck through which the diffusing cation has to pass [56]. As a result, the activation barriers to cation transport can be strongly influenced by dynamics of the anion framework [57,58]. This factor was proposed decades ago in high-temperature fast-ion conducting "plastic" phases consisting of tetrahedral polyanions – and while not well understood, was dubbed the paddle-wheel effect [59]. Indeed, early work on α-Li_2SO_4 speculated that the reorientational motion of the SO_4^{2-} anions above 850 K was responsible for the jump in Li^+ ion conductivity at that temperature [60]. Quasi-elastic neutron scattering (QENS) studies showed the PO_4^{3-} anions in Na_3PO_4 undergo rapid rotation in the fast-ion plastic phase above 600 K [61]. In the groundbreaking solid electrolyte, $Li_{10}GeP_2S_{12}$ [5], reorientation of the PS_4^- groups observed in high temperature AIMD simulations was related to cation transport [62]. While a full picture of the importance of polyanion rotational dynamics on cation diffusion in inorganic solids has taken time to develop - now - owing to advances in computational and physical methods, the coupling of anion and cation dynamics is better defined, and the paddle-wheel effect has been brought down to intermediate, and even room temperature [42,63-72].

Our definition of shells and cages in Figure 1 focuses on the solvation structure (shells and cages) in the immediate vicinity of the working ion. Since coulombic interactions can be significant over large distances, especially in low dielectric constant materials, the translation of the working ion may be affected by correlations between the working ion and entities outside the solvation structure. All relevant correlations are captured in the Onsager-Newman approach. One may view each term in the sum on the right side of Eq. 6 as an element of an $N_i \times N_j$ matrix. If the motion of a given ion is independent of all other entities, then the matrix is diagonal, and L_{ii} and D_i are proportional to each other (i = + or -) while L_{+-}=0. In general, however, L_{ij} are functions of sparse matrices wherein most of the elements are zero (or nearly so), as simulation boxes must be much larger than the characteristic length scales of the interspecies correlations. A simple estimate of distances that are relevant for transport is given by the Bjerrum length [73], defined as the separation distance between ions at which the coulombic energy equals thermal energy (k_BT). The Bjerrum lengths of water and PEO are 0.7 and 7 nm (the dielectric constants of water and PEO are 80.1 and 7.5). The number of non-negligible matrix elements contributing to L_{ij} will thus be larger for the PEO electrolyte (Figure 1d) relative to the aqueous electrolyte (Figure 1a). In all cases, however, the most significant off-diagonal elements of the matrices underlying L_{ij} are related to correlations between the working ion and entities in solvation shells and cages.

There are many approaches for studying the coupling between cage dynamics and ion transport. Analysis of neutron diffraction data using the maximum entropy method (MEM) can be used to reconstruct nuclear density maps; it provides a method to "peer into" the crystal to view a snapshot

of structural disorder and lattice dynamics. However, like QENS, it can only provide generalised and averaged information, from which a spatial and time-averaged structural picture can be obtained. Local correlation effects are not reflected. AIMD simulations provide powerful, complementary insights as they record the real-time dynamics of atoms on the femtosecond time scale. A combination of the two approaches, first explored in a new series of fast Na-ion conductors ($Na_{11}Sn_2PnX_{12}$: Pn = P, Sb; X = S, Se) [74], was applied to investigation of the crystalline LPS family. This study compared the high temperature fast-ion conductor (β-Li_3PS_4) with its room temperature Li-stuffed analogue, $Li_{3.25}[P_{3/4}Si_{1/4}]S_4$ [70]. AIMD, joint-time correlation analysis, and power spectra demonstrated that the PS_4^{3-}/SiS_4^{3-} anion rotational dynamics couple to and greatly enhance cation diffusion *via* the paddle-wheel effect; Figure 3. The transition from non-conductive γ-Li_3PS_4 to β-Li_3PS_4 coincides with the onset of PS_4^{3-} anion rotation. MEMS maps revealed that PS_4^{3-} anions are static in the γ-phase, but rotationally disordered in the β-phase. Partial substitution of P^{5+} with (Si^{4+} + Li^+) expands the cell volume, stabilizing the β-structure. This "turns on" anion rotation in Si-LPS at room temperature, giving rise to fast-ion conductivity of 1.2 mS cm^{-1} that represents a 1000-fold increase vs the γ-phase. AIMD simulations further showed that reducing the free volume by 10% hinders polyanion rotation, leading to higher rotational barrier heights and lower Li^+ diffusivity.

The effect of anion cage dynamics is to transiently open the bottleneck for cation transport. Because the PS_4^{3-} polyanions share bonds with the cages, during the AIMD picosecond snapshots where they rotate, the window through which the cations pass from one solvation cage to the other is enlarged by about 25%. This is accompanied by cation diffusion events that occur cooperatively with the rotation of the anions, and correlate with transport from one lattice site to the neighboring site. One can alternatively consider that rotation of the anion groups creates disorder in the anion framework, leading to fluctuating potentials and a frustrated energy landscape that the cations perceive. This lowers the activation energy for cation migration.

Regarding glassy Li_3PS_4, AIMD simulations show that the glass also shows reorientational anion dynamics at room temperature [42]. Connections between Li^+ migration and the rotational dynamics of the PS_4^{3-} anions in the glass were explored with AIMD by evaluating correlations in space and in time, and potential similarities in their respective energetics and vibrational properties. Figure 4 shows an example of a Li^+ migration event observed during the AIMD simulation. The left panel shows the trajectory for a cooperative migration process wherein three adjacent lithium ions migrate at approximately the same time. During this process a neighboring PS_4^{3-} anion undergoes a large, quasi-permanent reorientation, indicative of the paddle-wheel effect. Figure 4b demonstrates that the displacement of one of the Li^+ ions is strongly correlated in time with the reorientation of a PS_4^{3-} anion in the solvating cage. The distinct anion dynamics in the glassy state are ascribed to a combination of the lower density of the glass (due to imperfect ion packing in the amorphous state) and the absence of a long-ranged covalent (bridging) network. These two features provide the additional free volume needed to allow for anion rotation, while minimizing the formation of longer chain P_xS_y anions having less rotational mobility [42,75].

The rotational dynamics of complex anions can be quantified by calculating the anions' orientational autocorrelation function [33,42,63]. The resulting curve of correlation vs. time can be fit to an exponential form, $\exp(-t/\tau)$, where τ^{-1} represents the correlation frequency for rotational anion displacements. Importantly, these frequencies can also be extracted from QENS experiments, and thus provide a mechanism for directly comparing theory and experiments [63,76]. Finally, a plot of the anion orientation autocorrelation function (Figure 4) reveals that the anions are

rotationally active over the time scale of the simulation. In total, these analyses demonstrate a strong connection between the mobility of the Li^+ cation and the structure and mobility of its solvating cage.

The experimentally determined relationship between cage dynamics and ion transport in LiTFSI/PEO mixtures is shown in Figure 5. In Figure 5a, we show measurements of the time dependence of the mean-squared displacement of the PEO segments $< \Delta r_0^2(t) >$ measured by QENS [77]. On the 0.1 to 3 ns time scale, the motion is sub-diffusive at all salt concentrations as mentioned in Table 1, *i.e.*, $M = 0.5$ or $< \Delta r_0^2(t) >$ is proportional to $t^{1/2}$. The proportionality constant, D_0, in equation (1) gives the coefficient of friction that is experienced by the PEO segments, ζ; see ref. 61 for the explicit expression. The addition of salt results in smaller segment displacements or increased ζ in polymer electrolytes; it is customary to express salt concentration as r_s, the ratio of moles of salt to moles of ethylene oxide monomers. The data in Figure 5a indicate that ζ increases exponentially with r_s. These data reflect the displacement of polymer segments coordinated with the cations as well as those far away from the cations. While it is possible to study the motion of particular entities in simulations as has been done in Figures 3 and 4, continuum transport depends on the motion of all entities in the system. Thus, while the mobility of entities in the solvation cage is thus reflected indirectly in the $< \Delta r_0^2(t) >$ data measured by QENS in Figure 5, continuum properties like conductivity depend on these data.

In Figure 5b, we show experimentally measured conductivity κ as a function or r_s. The curve through the data is

$$\kappa = 0.043 r_s \, exp\left(-\frac{r_s}{0.085}\right) \text{ S/cm}, \quad (7)$$

where the linear prefactor represents the simple expectation that conductivity is proportional to the concentration of charges and the exponential term represents the increase in friction obtained entirely from analysis of the QENS data. In LiTFSI/PEO, conductivity, a parameter that reflects only the displacement of charged species is, in fact, governed by a hidden variable – the sub-diffusive motion of the cage comprising uncharged polymer segments. Here the coupling between cage dynamics and ion transport is exposed by combining QENS and standard ac impedance experiments.

Concluding remarks

Electrochemical systems with solid electrolytes may be ideally suited for clean energy technologies. In spite of the many advantages of solid electrolytes, they must embody many features that liquid electrolytes possess such as a wide electrochemical stability window and the ability to accommodate expansion and contraction of electrode particles. Our main objective is to begin establishing a unified framework for characterizing both solid and liquid electrolytes. We build upon the concepts of solvation shells and cages, showing geometric similarities between widely differing electrolytes (Figure 1). While the importance of the chemical composition of the solvating entities has long been recognized, there is an emerging recognition of the importance of the dynamics of these entities (Figure 2). We present three examples of solid electrolytes wherein the transport of the working cation is intimately related to these dynamical properties (Figures 3, 4, and 5). The unified framework that we seek to develop must be built upon order parameters that apply across the classes; we present cage and shell mobility as one such parameter. Table 1 gives this order parameter, along with the universally agreed upon metric for characterizing

continuum ion transport - conductivity. While we have focused on simulations, QENS and ac impedance, a variety of other theoretical and experimental approaches can be deployed to relate atomic-level information to continuum transport. The minimum number of order parameters that are necessary to construct our framework remains an open question, as are the nature of relationships between these parameters and continuum transport (see Outstanding Questions). In systems with two translationally mobile charged species and one neutral species such as liquid and polymer electrolytes, ion transport is governed by three transport parameters [78-80]. In the future, one may consider extensions to more complex systems such as polymer gels, wherein an ionic solution is imbibed within a polymer network, which contain two neutral species. We recognize the importance of interfacial effects; extending our framework to include them is a challenging but worthwhile exercise. Our ultimate goal is enabling the rational design of the solvation environment that propels the migration of the working ions.

Acknowledgements
This work was entirely supported by the Joint Center for Energy Storage Research (JCESR), an Energy Innovation Hub funded by the U.S. Department of Energy, Office of Science, Basic Energy Sciences. We acknowledge the JCESR community for their support, especially Zhou Yu, Jeff Smith, Kavish Kaup, Zhizhen Zhang, Laidong Zhu, Lei Cheng and Rui Wang.

Glossary

Amorphous halos: diffuse rings detected by X-ray or neutron scattering due to short-range correlations characteristic of amorphous liquids, polymers, and glasses.
Cages: a collection of nearest neighbors coordinated with a solvated ion that does not translate with the ion.
Cation transference number: the fraction of current carried by the cation relative to a reference velocity in an electrolyte of uniform composition; commonly used reference velocities are the mass-average velocity (used in Eq. 6), the molar-average velocity, and the solvent velocity.
Conductivity: a measure of the current obtained at the instant a potential is applied across an electrolyte with uniform composition.
Entities: ions and neutral molecules (monomers in the case of polymer electrolytes) that make up electrolytes.
Maximum entropy method: a model-free method to extract atomic positions from measured diffraction data.
Mobility order parameter: the ratio of the exponent quantifying the time dependence of the mean-squared displacement of the entities in shells and cages to that of the working ion.
Onsager coefficients, L_{ij}: coefficients that relate the flux of the species i to gradients in the chemical potentials of species j.
Salt diffusion coefficient: the proportionality factor that relates the flux density of salt to the concentration gradient.
Self-diffusion coefficient: a measure of the average mean-squared displacement of the species of interest per unit time.
Shells: a collection of nearest neighbors coordinated with an ion solvated in a liquid that translates with the ion for a short while before it breaks up due to Brownian motion.

References

1. Newman, J. and N. P. Balsara, (2021) *Electrochemical Systems.* 4th Ed., New York: Wiley.
2. Goodenough, J.B. and Park, K.-S. (2013) The Li-Ion Rechargeable Battery: A Perspective. *Journal of the American Chemical Society* 135, 1167-1176. 10.1021/ja3091438
3. Mizushima, K. *et al.* (1980) LixCoO2 (0<x<-1): A new cathode material for batteries of high energy density. *Materials Research Bulletin* 15, 783-789. https://doi.org/10.1016/0025-5408(80)90012-4
4. Trahey, L. *et al.* (2020) Energy storage emerging: A perspective from the Joint Center for Energy Storage Research. *Proceedings of the National Academy of Sciences* 117, 12550. 10.1073/pnas.1821672117
5. Kamaya, N. *et al.* (2011) A lithium superionic conductor. *Nature Materials* 10, 682-686. 10.1038/nmat3066
6. Seino, Y. *et al.* (2014) A sulphide lithium super ion conductor is superior to liquid ion conductors for use in rechargeable batteries. *Energy & Environmental Science* 7, 627-631. 10.1039/C3EE41655K
7. Kraft, M.A. *et al.* (2017) Influence of Lattice Polarizability on the Ionic Conductivity in the Lithium Superionic Argyrodites Li6PS5X (X = Cl, Br, I). *Journal of the American Chemical Society* 139, 10909-10918. 10.1021/jacs.7b06327
8. Zhou, L. *et al.* (2019) New Family of Argyrodite Thioantimonate Lithium Superionic Conductors. *Journal of the American Chemical Society* 141, 19002-19013. 10.1021/jacs.9b08357
9. Fuchs, T. *et al.* (2020) Defect-Mediated Conductivity Enhancements in Na3–xPn1–xWxS4 (Pn = P, Sb) Using Aliovalent Substitutions. *ACS Energy Letters* 5, 146-151. 10.1021/acsenergylett.9b02537
10. Adeli, P. *et al.* (2021) Influence of Aliovalent Cation Substitution and Mechanical Compression on Li-Ion Conductivity and Diffusivity in Argyrodite Solid Electrolytes. *Chemistry of Materials* 33, 146-157. 10.1021/acs.chemmater.0c03090
11. Jiang, C. *et al.* (2017) Recent progress in solid-state electrolytes for alkali-ion batteries. *Science Bulletin* 62, 1473-1490. https://doi.org/10.1016/j.scib.2017.10.011
12. Logan, E.R. and Dahn, J.R. (2020) Electrolyte Design for Fast-Charging Li-Ion Batteries. *Trends in Chemistry* 2, 354-366. 10.1016/j.trechm.2020.01.011
13. Li, J. *et al.* (2015) Solid Electrolyte: the Key for High-Voltage Lithium Batteries. *Advanced Energy Materials* 5, 1401408. https://doi.org/10.1002/aenm.201401408
14. Kato, Y. *et al.* (2016) High-power all-solid-state batteries using sulfide superionic conductors. *Nature Energy* 1, 16030. 10.1038/nenergy.2016.30
15. Randau, S. *et al.* (2020) Benchmarking the performance of all-solid-state lithium batteries. *Nature Energy* 5, 259-270. 10.1038/s41560-020-0565-1
16. Sun, Y.-K. (2020) Promising All-Solid-State Batteries for Future Electric Vehicles. *ACS Energy Letters* 5, 3221-3223. 10.1021/acsenergylett.0c01977
17. Sharafi, A. *et al.* (2017) Surface Chemistry Mechanism of Ultra-Low Interfacial Resistance in the Solid-State Electrolyte Li7La3Zr2O12. *Chemistry of Materials* 29, 7961-7968. 10.1021/acs.chemmater.7b03002
18. Monroe, C. and Newman, J. (2005) The Impact of Elastic Deformation on Deposition Kinetics at Lithium/Polymer Interfaces. *Journal of The Electrochemical Society* 152, A396. 10.1149/1.1850854

19. Wolfenstine, J. *et al.* (2018) Mechanical behavior of Li-ion-conducting crystalline oxide-based solid electrolytes: a brief review. *Ionics* 24, 1271-1276. 10.1007/s11581-017-2314-4
20. Nagy, K.S. and Siegel, D.J. (2020) Anisotropic Elastic Properties of Battery Anodes. *Journal of The Electrochemical Society* 167, 110550. 10.1149/1945-7111/aba54c
21. Koerver, R. *et al.* (2018) Chemo-mechanical expansion of lithium electrode materials – on the route to mechanically optimized all-solid-state batteries. *Energy & Environmental Science* 11, 2142-2158. 10.1039/C8EE00907D
22. Yu, S. and Siegel, D.J. (2018) Grain Boundary Softening: A Potential Mechanism for Lithium Metal Penetration through Stiff Solid Electrolytes. *ACS Applied Materials & Interfaces* 10, 38151-38158. 10.1021/acsami.8b17223
23. Albertus, P. *et al.* (2018) Status and challenges in enabling the lithium metal electrode for high-energy and low-cost rechargeable batteries. *Nature Energy* 3, 16-21. 10.1038/s41560-017-0047-2
24. Porz, L. *et al.* (2017) Mechanism of Lithium Metal Penetration through Inorganic Solid Electrolytes. *Advanced Energy Materials* 7, 1701003. https://doi.org/10.1002/aenm.201701003
25. Liu, J. *et al.* (2019) Pathways for practical high-energy long-cycling lithium metal batteries. *Nature Energy* 4, 180-186. 10.1038/s41560-019-0338-x
26. Kasemchainan, J. *et al.* (2019) Critical stripping current leads to dendrite formation on plating in lithium anode solid electrolyte cells. *Nature Materials* 18, 1105-1111. 10.1038/s41563-019-0438-9
27. Li, G. and Monroe, C.W. (2019) Dendrite nucleation in lithium-conductive ceramics. *Physical Chemistry Chemical Physics* 21, 20354-20359. 10.1039/C9CP03884A
28. Harris, W.S. (1958). Electrochemical Studies in Cyclic Esters. University of California, Berkeley
29. Yu, Z. *et al.* (2020) Asymmetric Composition of Ionic Aggregates and the Origin of High Correlated Transference Number in Water-in-Salt Electrolytes. *The Journal of Physical Chemistry Letters* 11, 1276-1281. 10.1021/acs.jpclett.9b03495
30. Han, K.S. *et al.* (2020) Origin of Unusual Acidity and Li+ Diffusivity in a Series of Water-in-Salt Electrolytes. *The Journal of Physical Chemistry B* 124, 5284-5291. 10.1021/acs.jpcb.0c02483
31. Liu, Z. *et al.* (2013) Anomalous High Ionic Conductivity of Nanoporous β-Li3PS4. *Journal of the American Chemical Society* 135, 975-978. 10.1021/ja3110895
32. Kaup, K. *et al.* (2020) Impact of the Li substructure on the diffusion pathways in alpha and beta Li3PS4: an in situ high temperature neutron diffraction study. *Journal of Materials Chemistry A* 8, 12446-12456. 10.1039/D0TA02805C
33. Zhou, L. *et al.* (2019) An Entropically Stabilized Fast-Ion Conductor: Li3.25[Si0.25P0.75]S4. *Chemistry of Materials* 31, 7801-7811. 10.1021/acs.chemmater.9b00657
34. Angell, C.A. (1983) Fast ion motion in glassy and amorphous materials. *Solid State Ionics* 9-10, 3-16. https://doi.org/10.1016/0167-2738(83)90206-0
35. Ravaine, D. (1980) Glasses as solid electrolytes. *Journal of Non-Crystalline Solids* 38-39, 353-358. https://doi.org/10.1016/0022-3093(80)90444-5
36. Hayashi, A. *et al.* (2012) Superionic glass-ceramic electrolytes for room-temperature rechargeable sodium batteries. *Nature Communications* 3, 856. 10.1038/ncomms1843

37. Donati, C. *et al.* (1999) Spatial correlations of mobility and immobility in a glass-forming Lennard-Jones liquid. *Physical Review E* 60, 3107-3119
38. Angell, C.A. *et al.* (2000) Relaxation in glassforming liquids and amorphous solids. *Journal of Applied Physics* 88, 3113-3157. 10.1063/1.1286035
39. Ediger, M.D. (2000) Spatially Heterogeneous Dynamics in Supercooled Liquids. *Annual Review of Physical Chemistry* 51, 99-128. 10.1146/annurev.physchem.51.1.99
40. Stillinger, F.H. (1995) A Topographic View of Supercooled Liquids and Glass Formation. *Science* 267, 1935. 10.1126/science.267.5206.1935
41. Ohara, K. *et al.* (2016) Structural and electronic features of binary Li2S-P2S5 glasses. *Scientific Reports* 6, 21302. 10.1038/srep21302
42. Smith, J.G. and Siegel, D.J. (2020) Low-temperature paddlewheel effect in glassy solid electrolytes. *Nature Communications* 11, 1483. 10.1038/s41467-020-15245-5
43. Fenton, D.E. *et al.* (1973) Complexes of alkali metal ions with poly(ethylene oxide). *Polymer* 14, 589. https://doi.org/10.1016/0032-3861(73)90146-8
44. Armand, M.B. (1986) Polymer Electrolytes. *Annual Review of Materials Science* 16, 245-261. 10.1146/annurev.ms.16.080186.001333
45. Borodin, O. and Smith, G.D. (2006) Mechanism of Ion Transport in Amorphous Poly(ethylene oxide)/LiTFSI from Molecular Dynamics Simulations. *Macromolecules* 39, 1620-1629. 10.1021/ma052277v
46. Doi, M. (2015) *Soft Matter Physics* Oxford University Press
47. Lascaud, S. *et al.* (1994) Phase Diagrams and Conductivity Behavior of Poly(ethylene oxide)-Molten Salt Rubbery Electrolytes. *Macromolecules* 27, 7469-7477. 10.1021/ma00103a034
48. Fang, C. *et al.* (2021) Salt Activity Coefficient and Chain Statistics in Poly(ethylene oxide)-Based Electrolytes. *Macromolecules*. 10.1021/acs.macromol.0c01850
49. Onsager, L. (1945) THEORIES AND PROBLEMS OF LIQUID DIFFUSION. *Annals of the New York Academy of Sciences* 46, 241-265. https://doi.org/10.1111/j.1749-6632.1945.tb36170.x
50. France-Lanord, A. and Grossman, J.C. (2019) Correlations from Ion Pairing and the Nernst-Einstein Equation. *Physical Review Letters* 122, 136001. 10.1103/PhysRevLett.122.136001
51. Molinari, N. *et al.* (2019) General Trend of a Negative Li Effective Charge in Ionic Liquid Electrolytes. *The Journal of Physical Chemistry Letters* 10, 2313-2319. 10.1021/acs.jpclett.9b00798
52. Harris, K.R. (2010) Relations between the Fractional Stokes−Einstein and Nernst−Einstein Equations and Velocity Correlation Coefficients in Ionic Liquids and Molten Salts. *The Journal of Physical Chemistry B* 114, 9572-9577. 10.1021/jp102687r
53. Dong, D. *et al.* (2018) How efficient is Li+ ion transport in solvate ionic liquids under anion-blocking conditions in a battery? *Physical Chemistry Chemical Physics* 20, 29174-29183. 10.1039/C8CP06214E
54. Wheeler, D.R. and Newman, J. (2004) Molecular Dynamics Simulations of Multicomponent Diffusion. 1. Equilibrium Method. *The Journal of Physical Chemistry B* 108, 18353-18361. 10.1021/jp047850b
55. Vargas-Barbosa, N.M. and Roling, B. (2020) Dynamic Ion Correlations in Solid and Liquid Electrolytes: How Do They Affect Charge and Mass Transport? *ChemElectroChem* 7, 367-385. https://doi.org/10.1002/celc.201901627

56. Wang, Y. *et al.* (2015) Design principles for solid-state lithium superionic conductors. *Nature Materials* 14, 1026. 10.1038/nmat4369
https://www.nature.com/articles/nmat4369#supplementary-information
57. Muy, S. *et al.* (2020) Phonon–Ion Interactions: Designing Ion Mobility Based on Lattice Dynamics. *Advanced Energy Materials* n/a, 2002787. https://doi.org/10.1002/aenm.202002787
58. Fang, H. and Jena, P. (2017) Li-rich antiperovskite superionic conductors based on cluster ions. *Proceedings of the National Academy of Sciences* 114, 11046. 10.1073/pnas.1704086114
59. Jansen, M. (1991) Volume Effect or Paddle-Wheel Mechanism—Fast Alkali-Metal Ionic Conduction in Solids with Rotationally Disordered Complex Anions. *Angewandte Chemie International Edition in English* 30, 1547-1558. 10.1002/anie.199115471
60. Aronsson, R. *et al.* (1980) Fast ion conductors with rotating sulphate ions. *J. Phys. Colloques* 41, C6-35-C36-37
61. Wilmer, D. *et al.* (1999) Anion reorientation in an ion conducting plastic crystal – coherent quasielastic neutron scattering from sodium ortho-phosphate. *Physica B: Condensed Matter* 266, 60-68. https://doi.org/10.1016/S0921-4526(98)01494-X
62. Adams, S. and Prasada Rao, R. (2012) Structural requirements for fast lithium ion migration in Li10GeP2S12. *Journal of Materials Chemistry* 22, 7687-7691. 10.1039/C2JM16688G
63. Dimitrievska, M. *et al.* (2018) Carbon Incorporation and Anion Dynamics as Synergistic Drivers for Ultrafast Diffusion in Superionic LiCB11H12 and NaCB11H12. *Advanced Energy Materials* 8, 1703422. https://doi.org/10.1002/aenm.201703422
64. Famprikis, T. *et al.* (2019) A New Superionic Plastic Polymorph of the Na+ Conductor Na3PS4. *ACS Materials Letters* 1, 641-646. 10.1021/acsmaterialslett.9b00322
65. Klein, I.S. *et al.* (2018) A New Version of the Lithium Ion Conducting Plastic Crystal Solid Electrolyte. *Advanced Energy Materials* 8, 1801324. https://doi.org/10.1002/aenm.201801324
66. Kweon, K.E. *et al.* (2017) Structural, Chemical, and Dynamical Frustration: Origins of Superionic Conductivity in closo-Borate Solid Electrolytes. *Chemistry of Materials* 29, 9142-9153. 10.1021/acs.chemmater.7b02902
67. Sun, Y. *et al.* (2019) Rotational Cluster Anion Enabling Superionic Conductivity in Sodium-Rich Antiperovskite Na3OBH4. *Journal of the American Chemical Society* 141, 5640-5644. 10.1021/jacs.9b01746
68. Udovic, T.J. *et al.* (2014) Exceptional Superionic Conductivity in Disordered Sodium Decahydro-closo-decaborate. *Advanced Materials* 26, 7622-7626. https://doi.org/10.1002/adma.201403157
69. Wang, F. *et al.* (2020) Dynamics of Hydroxyl Anions Promotes Lithium Ion Conduction in Antiperovskite Li2OHCl. *Chemistry of Materials* 32, 8481-8491. 10.1021/acs.chemmater.0c02602
70. Zhang, Z. *et al.* (2020) Targeting Superionic Conductivity by Turning on Anion Rotation at Room Temperature in Fast Ion Conductors. *Matter* 2, 1667-1684. 10.1016/j.matt.2020.04.027
71. Zhang, Z. *et al.* (2019) Coupled Cation–Anion Dynamics Enhances Cation Mobility in Room-Temperature Superionic Solid-State Electrolytes. *Journal of the American Chemical Society* 141, 19360-19372. 10.1021/jacs.9b09343

72. Song, A.-Y. *et al.* (2018) Protons Enhance Conductivities in Lithium Halide Hydroxide/Lithium Oxyhalide Solid Electrolytes by Forming Rotating Hydroxy Groups. *Advanced Energy Materials* 8, 1700971. https://doi.org/10.1002/aenm.201700971
73. N, B. (1926) Ionic association. I. Influence of ionic association on the activity of ions at moderate degrees of association. *Danske Vid Selskab. Math-fys medd* 7, 1-48
74. Zhang, Z. *et al.* (2018) Na11Sn2PS12: a new solid state sodium superionic conductor. *Energy & Environmental Science* 11, 87-93. 10.1039/C7EE03083E
75. Dietrich, C. *et al.* (2017) Lithium ion conductivity in Li2S–P2S5 glasses – building units and local structure evolution during the crystallization of superionic conductors Li3PS4, Li7P3S11 and Li4P2S7. *Journal of Materials Chemistry A* 5, 18111-18119. 10.1039/C7TA06067J
76. Myrdal, J.S.G. *et al.* (2013) Li-ion Conduction in the LiBH4:LiI System from Density Functional Theory Calculations and Quasi-Elastic Neutron Scattering. *The Journal of Physical Chemistry C* 117, 9084-9091. 10.1021/jp311980h
77. Mongcopa, K.I.S. *et al.* (2018) Relationship between Segmental Dynamics Measured by Quasi-Elastic Neutron Scattering and Conductivity in Polymer Electrolytes. *ACS Macro Letters* 7, 504-508. 10.1021/acsmacrolett.8b00159
78. Ma, Y. *et al.* (1995) The Measurement of a Complete Set of Transport Properties for a Concentrated Solid Polymer Electrolyte Solution. *Journal of The Electrochemical Society* 142, 1859-1868. 10.1149/1.2044206
79. Pesko, D.M. *et al.* (2017) Negative Transference Numbers in Poly(ethylene oxide)-Based Electrolytes. *Journal of The Electrochemical Society* 164, E3569-E3575. 10.1149/2.0581711jes
80. Landesfeind, J. and Gasteiger, H.A. (2019) Temperature and Concentration Dependence of the Ionic Transport Properties of Lithium-Ion Battery Electrolytes. *Journal of The Electrochemical Society* 166, A3079-A3097. 10.1149/2.0571912jes

Figure Captions.

Figure 1. Solvation structures of lithium ions in liquid and solid electrolytes. (a) LiTFSI in water at 298 K. (b) β-Li_3PS_4 crystal, stable above 573 K. (c) Amorphous Li_3PS_4 glass at 298 K. (d) LiTFSI in polyethylene oxide at 363 K. In (a) H is blue, O is red, Li is green, and TFSI is yellow. In (b) and (c) Li is green, P is purple, and S is yellow. In (d) CH_2 is blue, O is red, Li is green, and TFSI is yellow. The solvation shell and cage in liquid and polymer electrolytes are indicated by a green polyhedron surrounding the lithium ion.

Figure 2. Ion diffusion and dynamics of solvation shells and cages. Mean-squared displacement of the working ion and elements of shells and cages, $\langle \Delta r_i^2 \rangle$, versus time in different electrolytes. Mean-squared angular displacement of the anion, $\langle \Delta \theta_-^2 \rangle$, versus time is also shown for the glass in (c). (a) Schematic plot showing different systems. (b-d) Simulation results for translational and rotational displacement. (b) Liquid electrolyte, LiTFSI/water, 298 K. (c) 75% Li_2S and 25% P_2S_5 glass, 500 K. (d) Polymer electrolyte, LiTFSI/PEO, 363 K. Dashed lines in (b-d) represent expected power laws.

Figure 3. Relationship between cage dynamics and ion transport in a crystal, $Li_{3.25}[Si_{0.25}P_{0.75}]S_4$. (a) Trajectories of the S^{2-} ligands of $[PnS_4]$ (Pn = Si/P) polyanions from AIMD simulation; yellow spheres: initial position of S atoms; orange, blue, green, and purple spheres: S trajectories. The trajectories of Li^+ in the vicinity of one $[PnS_4]$ within 1 ps at 1050 K: (b) when $[PnS_4]$ is undergoing rotation; (c) when $[PnS_4]$ rotation pauses. The coordinates of one Li^+ in the vicinity of the $[PnS_4]$: (d) during its rotation; (e) when the anion rotation pauses. (f) A schematic showing the effect of the polyanion rotation on the trigonal bottleneck that Li^+ ions hop through; blue circles represent S atoms shared by the $[PnS_4]$ tetrahedron and the $[LiS_4]$ or $[LiS_6]$. Red and blue arrows depict pathways for Li^+ migration derived from AIMD simulation, and green arrows show the Li^+-ion path through the triangular face-sharing windows. (g) The area of the trigonal bottleneck for Li^+ migration when $[PnS_4]$ undergoes rotation and when rotation pauses.

Figure 4. Relationship between cage dynamics and ion transport in glassy Li_3PS_4. (a) Li^+ migration event involving the displacement of 3 Li^+ ions and a neighboring PS_4^{3-} anion in LPS glass. The anion's position before and after migration is shown with transparent and opaque shading, respectively. (b) The displacement of one of the Li^+ ion involved in this migration event (black curve) and the orientation of 3 neighboring PS_4^{3-} anions (blue curves) during the migration event as a function of time. (c) PS_4^{3-} anion orientation autocorrelation as a function of time at selected temperatures.

Figure 5. Relationship between cage dynamics and ion transport in a polymer electrolyte, LiTFSI/PEO. (a) Mean-squared displacement of PEO segments versus time at various salt concentrations, r_s, measured by QENS, showing cage dynamics with $M = 0.5$. (b) Measurements

of the dependence of conductivity on salt concentration (squares) explained entirely on a model that is based on cage dynamics (curve).

Figures.

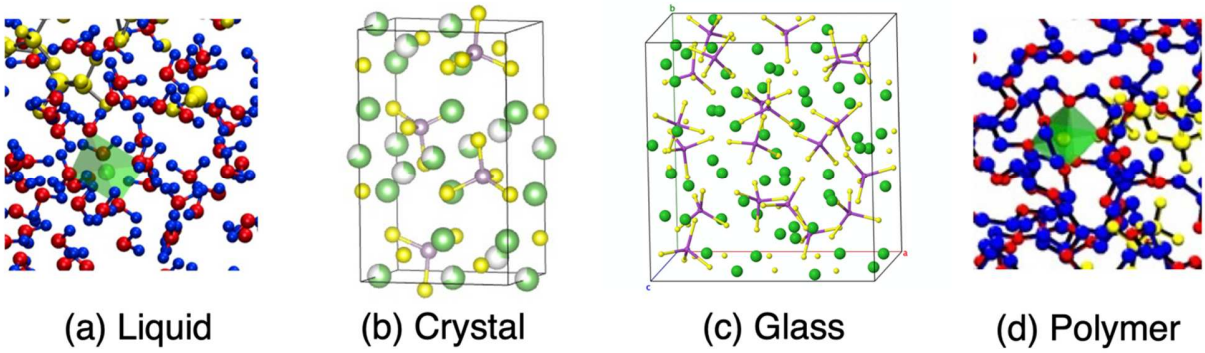

Figure 1.

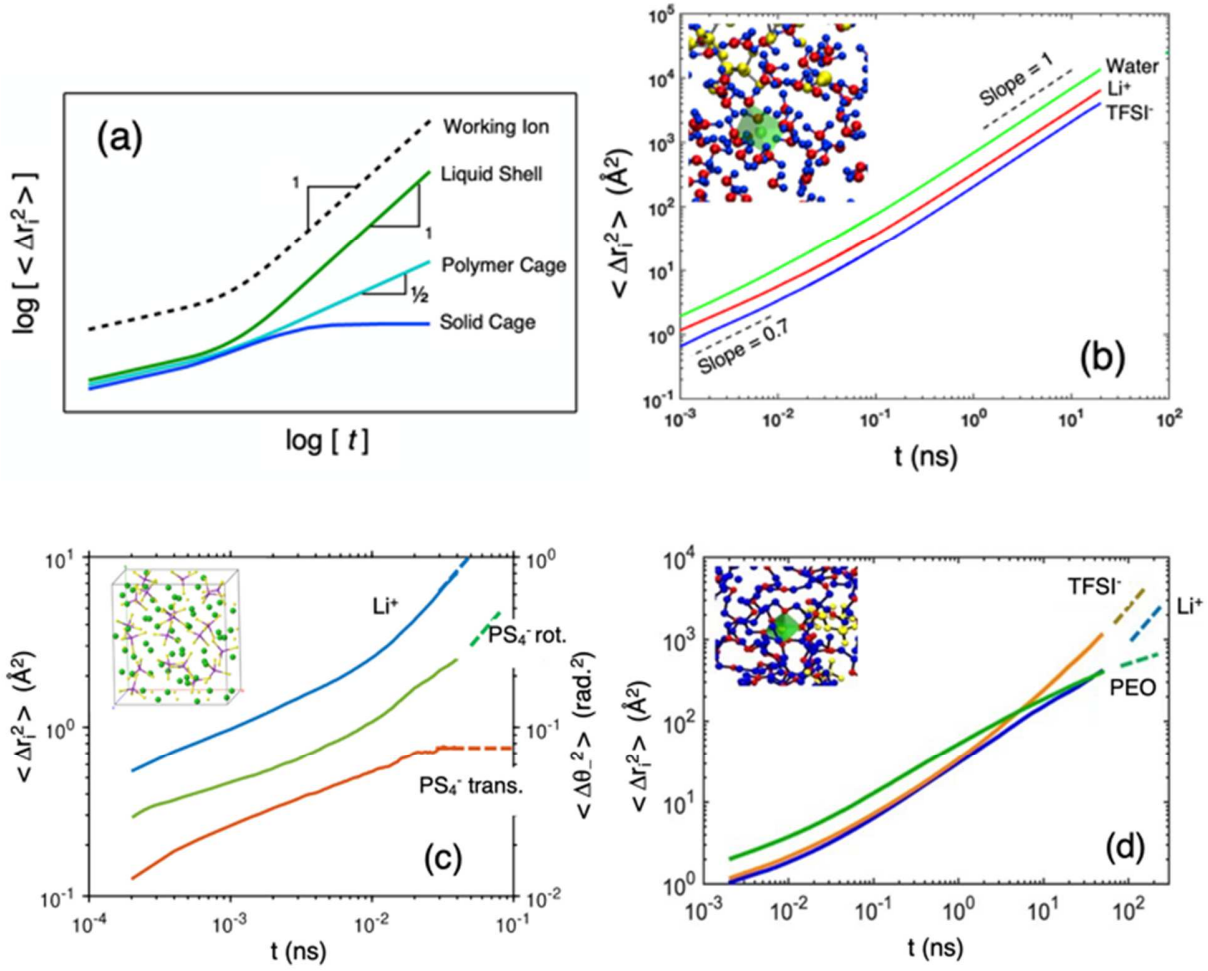
(a)
Working Ion
Liquid Shell
Polymer Cage
Solid Cage
1
1
½
log [< Δr_i^2 >]
log [t]
(b)
Water
Li+
TFSI-
Slope = 1
Slope = 0.7
< Δr_i^2 > (Å^2)
t (ns)
(c)
Li+
PS4- rot.
PS4- trans.
< Δr_i^2 > (Å^2)
< Δθ_2 > (rad.^2)
t (ns)
(d)
TFSI-
Li+
PEO
< Δr_i^2 > (Å^2)
t (ns)

Figure 2.

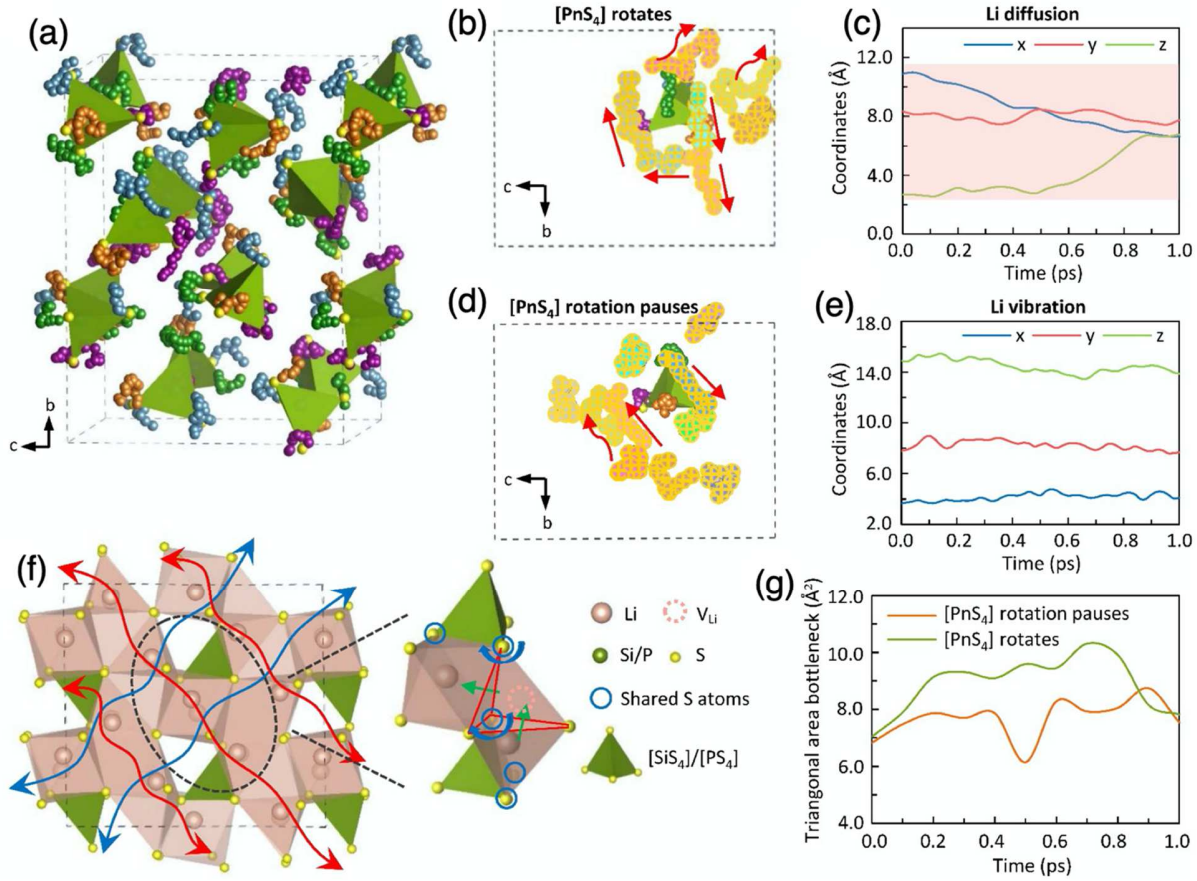
(a)
b
c
(b)
[PnS4] rotates
c
b
(c)
Li diffusion
x
y
z
Coordinates (Å)
12.0
8.0
4.0
0.0
0.0
0.2
0.4
0.6
0.8
1.0
Time (ps)
(d)
[PnS4] rotation pauses
c
b
(e)
Li vibration
x
y
z
Coordinates (Å)
18.0
14.0
10.0
6.0
2.0
0.0
0.2
0.4
0.6
0.8
1.0
Time (ps)
(f)
Li
VLi
Si/P
S
Shared S atoms
[SiS4]/[PS4]
(g)
[PnS4] rotation pauses
[PnS4] rotates
Triangonal area bottleneck (Å2)
12.0
10.0
8.0
6.0
4.0
0.0
0.2
0.4
0.6
0.8
1.0
Time (ps)

Figure 3.

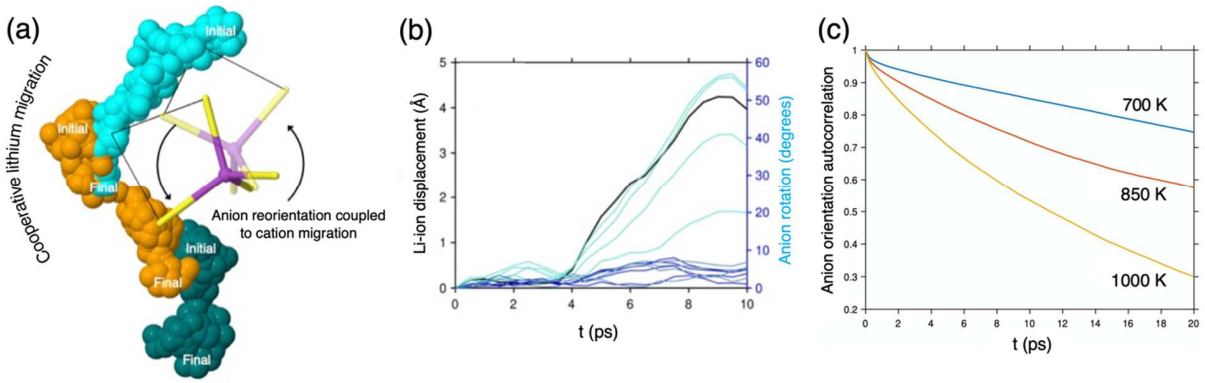
(a)
Cooperative lithium migration
Initial
Initial
Final
Anion reorientation coupled
to cation migration
Initial
Final
Final
(b)
Li-ion displacement (Å)
Anion rotation (degrees)
t (ps)
(c)
Anion orientation autocorrelation
700 K
850 K
1000 K
t (ps)

Figure 4.

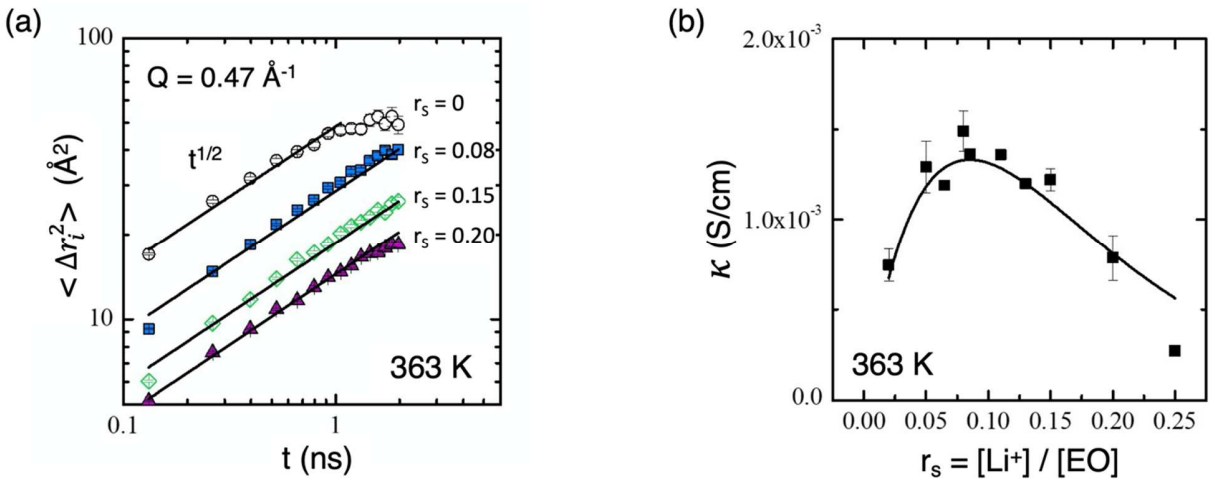
(a)
100
10
0.1
1
t (ns)
< Δr_i^2 > (Å^2)
Q = 0.47 Å^-1
t^1/2
r_s = 0
r_s = 0.08
r_s = 0.15
r_s = 0.20
363 K
(b)
2.0x10^-3
1.0x10^-3
0.0
κ (S/cm)
0.00 0.05 0.10 0.15 0.20 0.25
r_s = [Li+] / [EO]
363 K

Figure 5.

Table 1. Solvation, mobility order parameter, and conductivity of exemplar liquid and solid electrolytes.

Systems	Solvation Structure	Mobility Order Parameter	Conductivity (S/cm)
Liquids LiTFSI/water 0.2 M, 298K	Shell	$M = 1$	$3x10^{-2}$
Polymers LiTFSI/PEO 1.6 M, 363 K	Cage	$M = 0.5$	$2x10^{-3}$
Crystals $Li_{3.25}[P_{3/4}Si_{1/4}]S_4$ 298 K	Cage	$M = 0, M_\theta = 1$	$1x10^{-3}$
Inorganic Glasses LPS 298 K	Cage	$M = 0, M_\theta = 1$	$2x10^{-4}$